ACES Asian Chemical Editorial Society

doi.org/10.1002/cnma.202500270

CHEMNANOMAT
Research Article

www.chemnanomat.org

Micelle-Assisted Electrodeposition of γ-MnO_2 on Lead Anodes: Structural and Electrochemical Insights

Manickam Minakshi,* Rob Aughterson, Parul Sharma, Anurag Prakash Sunda, Katsuhiko Ariga, and Lok Kumar Shrestha

Electrolysis of $MnSO_4$ in H_2SO_4 with cationic surfactants (tetradecyltrimethylammonium bromide; TTAB and cetyltrimethylammonium bromide; CTAB) led to the formation of γ-MnO_2 with surfactant intercalation in an amorphous matrix. Unlike conventional self-standing EMD electrodes, which limit scalability, this study presents bulk electrodeposition of EMD powder on a lead (Pb) anode. Surface morphology is significantly altered by surfactant presence, though X-ray diffraction and density functional theory analyzes confirms consistent γ-MnO_2 crystallography across samples. Galvanostatic charge–discharge at 0.6 A g^{-1} reveals that TTAB-assisted EMD achieved a specific capacitance of 478.6 F g^{-1}, double that of pristine EMD (232 F g^{-1}), due to improved ion transport and surface area. In contrast, CTAB-assisted EMD shows reduced capacitance (124.6 F g^{-1}), attributed to early micelle formation and immobilization within the MnO_2 lattice, which promoted SO_4^{2-} insertion over surfactant deintercalation. Surfactant critical micelle concentrations and surface activity are key to electrochemical behavior in 1 M Na_2SO_4. An asymmetric device using TTAB-EMD as the cathode and activated carbon as the anode delivered 106 F g^{-1} and 40 Wh kg^{-1}, demonstrating practical viability. Band structure calculations support the experimental findings, indicating favorable electronic properties for charge storage.

1. Introduction

The transition to renewable energy sources such as solar, wind, and tidal power has intensified the need for advanced energy storage systems capable of mitigating the inherent intermittency of these resources. While conventional electrochemical storage systems like batteries and capacitors[1–9] have served this role, their limitations, particularly in terms of power density, cycle life, and environmental impact, have catalyzed the development of next-generation hybrid energy storage technologies.[10,11] This work addresses these challenges by engineering a high-performance hybrid supercapacitor that integrates the rapid charge–discharge characteristics of capacitive materials with the high energy density of battery-type electrodes.[12,13]

In commercial supercapacitors, activated carbon is commonly used as the electrode material, paired with various salts dissolved in organic solvents serving as electrolytes. Carbon-based electrodes are well-suited for energy storage applications due to their desirable properties, including excellent chemical and thermal stability, high electrical conductivity, and large surface area.[14] Electrochemical double-layer capacitors (EDLCs) utilizing activated carbon represent the most basic and widely available type of supercapacitor. However, in practical applications, their capacitance typically ranges from 100 to 250 F g^{-1}, with a relatively low energy density of 3 to 10 Wh kg^{-1}, which may be insufficient for more demanding energy storage requirements.[15] To address this limitation and enhance energy density, the present study explores the fabrication of a hybrid supercapacitor, as reported in the literature,[16] incorporating two electrodes with distinct charge storage mechanisms: one capacitive and the other battery-type. Specifically, this study explores the fabrication and electrochemical performance of an asymmetric hybrid

M. Minakshi
College of Science, Technology, Engineering & Mathematics
Murdoch University
Perth, Western Australia 6150, Australia
E-mail: minakshi@murdoch.edu.au

M. Minakshi, K. Ariga, L. K. Shrestha
Research Center for Materials Nanoarchitectonics (MANA)
National Institute for Materials Science (NIMS)
Tsukuba 305 0044, Japan

R. Aughterson
ANSTO, Materials, Menai
Australian Nuclear Science and Technology Organization
Menai, New South Wales 2232, Australia

P. Sharma, A. P. Sunda
Department of Chemistry
J. C. Bose University of Science and Technology
YMCA, Faridabad 121006, India

K. Ariga
Department of Advanced Materials Science, Graduate School of Frontier Sciences
The University of Tokyo
5-1-5 Kashiwanoha, Kashiwa, Chiba 277-8561, Japan

L. K. Shrestha
Department of Materials Science, Institute of Pure and Applied Sciences
University of Tsukuba
1-1, Tennodai, Tsukuba, Ibaraki 305-8573, Japan

Supporting information for this article is available on the WWW under https://doi.org/10.1002/cnma.202500270

capacitor composed of a faradaic electrode, electrolytic manganese dioxide (EMD, γ-MnO_2), paired with a carbon-based electrode.

Manganese dioxides (MnO_2) used in energy storage are classified as natural, chemical, or electrolytic. Since Leclanché's 1866 galvanic cell, MnO_2 has been a key component in dry cells[17] and remains widely used in alkaline batteries. EMD is preferred for its higher purity and superior properties.[9] EMD is valued not only as a cathode in lithium, sodium, and alkaline batteries but also as a catalyst in hydrogen production and supercapacitors. It offers a low-cost, nontoxic, high-energy-density alternative to Ni-, Co-, and V-based oxides. The γ-MnO_2 form, known for its structural versatility, enables intercalation of various metal cations.[17,18]

MnO_2 supports multiple redox transitions (Mn^{3+}/Mn^{2+}, Mn^{4+}/Mn^{3+}, Mn^{6+}/Mn^{4+}),[19] contributing to its pseudocapacitive behavior. Among manganese oxides (MnO, Mn_2O_3, Mn_3O_4, MnO_2, MnOx), MnO_2 is favored for its reversible Mn^{4+}/Mn^{3+} redox couple. MnO_2 also exists in various polymorphic forms, such as hollandite (α), pyrolusite (β), intergrowth (γ), birnessite (δ), and defect spinel (λ).[20] The EMD discussed in this work primarily consists of γ-MnO_2, an intergrowth of pyrolusite and ramsdellite phases in a 42:58 ratio, respectively.[21] These polymorphs significantly influence specific capacitance, which follows the trend: $\beta < \lambda < \gamma < \delta$.[22] In the γ-phase, EMD can reversibly intercalate hydrated alkali metal cations (e.g., Li^+, Na^+, K^+), with partial substitution of Mn^{4+} by Mn^{3+} to maintain charge neutrality.[18]

The novelty of this work lies in the strategic exploitation of the redox transitions among Mn^{4+}/Mn^{3+} and Mn^{3+}/Mn^{2+}, which facilitate reversible charge storage through surface and bulk faradaic reactions. This mechanism significantly enhances the specific capacitance and energy density beyond that of traditional EDLCs based on activated carbon, which are limited by purely electrostatic charge storage.

In this study, EMD was synthesized electrochemically by electrolyzing manganese sulfate in a sulfuric acid bath containing 50 g dm^{-3} Mn and 25 g dm^{-3} H_2SO_4, under an anodic current density of 200 A m^{-2}. The anodic oxidation of Mn^{2+} to MnO_2 was carried out using a lead (Pb) anode positioned parallel to a stainless-steel (SS) cathode. The anodic reaction is represented by Equation (1).

$$Mn^{2+} + 2H_2O \rightarrow MnO_2 + 4H^+ + 2e \quad (1)$$

To control the nucleation and tailor the morphology of electrodeposited MnO_2, surfactants are commonly introduced into the electrolyte as structure-directing agents or soft templates.[23,24] In this work, two cationic surfactants, namely cetyltrimethylammonium bromide (CTAB; $C_{16}H_{33}N(CH_3)_3Br$), and tetradecyltrimethylammonium bromide (TTAB; $C_{14}H_{29}N(CH_3)_3Br$),[25] were individually employed to electrodeposit MnO_2 from the manganese sulfate-sulfuric acid bath. The resulting EMD samples, intercalated with CTAB or TTAB, were evaluated to determine the trade-off between surfactant concentration and energy storage performance. CTAB, with a longer hydrophobic tail (C16), tends to aggregate at lower concentrations,[25–27] promoting its immobilization within the EMD matrix. This can lead to reduced discharge capacitance due to SO_4^{2-} anion insertion for charge compensation, which inhibits the de/intercalation of CTA^+ cations. In contrast, TTAB, with a shorter hydrophobic chain (C14), facilitates the extraction of TTA^+ cations into the electrolyte. Consequently, Na^+ ions from the Na_2SO_4 electrolyte are reversibly inserted into the EMD structure for charge compensation.[28,29] The experimental findings are supported and interpreted through theoretical analysis.

The resulting hybrid device (EMD|| AC; activated carbon) exhibits improved energy and power densities (16 Wh Kg^{-1} at 5780 W Kg^{-1}), extended cycle life with a retention of 96.2% of its initial capacitance after 5000 repeated cycles, and environmental compatibility, positioning it as a viable candidate for scalable, high-performance energy storage applications in renewable energy integration and portable electronics.

2. Results and Discussion

2.1. Electrochemical Synthesis (Electrodeposition) of γ-MnO_2

X-ray diffraction (XRD) analysis of EMD samples synthesized with different cationic surfactants, CTAB and TTAB, revealed minimal variation in crystalline phases compared to the pristine sample prepared without additives. However, field emission scanning electron microscopy (FESEM) images demonstrated pronounced differences in surface structure, morphology, and particle size distribution. As shown in **Figure 1**a, the pristine EMD exhibits spindle-shaped, aggregated particles forming a net-like morphology. These needlelike microstructures are densely packed and homogeneously distributed. In contrast, the incorporation of cationic surfactants during synthesis significantly altered the surface morphology of EMD, as illustrated in Figure 1b,c. The self-assembling nature of the surfactants plays a crucial role in directing the structural evolution of the material. The CTAB-modified sample (Figure 1b) displays a hierarchical lamellar architecture composed of compact sow-thistle-like formations and a porous network with vesicular features. This morphology suggests that weakened interactions among the charged head groups of CTAB may facilitate the immobilization of CTA^+ cations within the EMD matrix. On the other hand, the TTAB-modified sample (Figure 1c) exhibits elongated, spherical particles, indicative of increased water incorporation and a more loosely packed structure. The hydrophobic character of TTAB likely promotes the extraction of TTA^+ molecules into the solution, accompanied by Na^+ ion intercalation to maintain charge neutrality. These morphological transformations, driven by surfactant modulation,

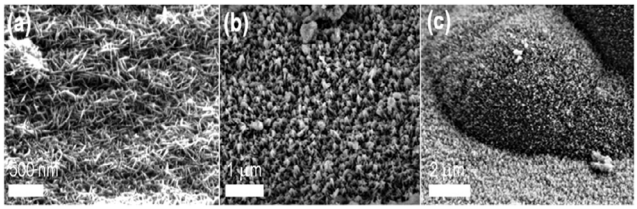

Figure 1. a) FESEM of (a) pristine EMD compared with EMD modified with two cationic surfactants, b) cetyltrimethylammonium bromide (CTAB), and c) tetradecyltrimethylammonium bromide (TTAB).

can enhance the electrochemical storage performance of EMD by introducing Mn vacancies that favor ion adsorption.[30]

The atomic-level internal structure of the EMD samples was examined using high-resolution transmission electron microscopy, as shown in **Figure 2**. The particles exhibited variability in both size and morphology, typically ranging from 10 to 20 nm. In the presence of cationic surfactants during electrodeposition, Figure 2e–h, i–l reveal surface-induced particle coalescence. This behavior is attributed to the hydrophobic nature of the surfactants, which influences the nucleation process. In contrast, the pristine EMD samples (Figure 2a–d) display spindle-shaped particles with no signs of coalescence, although slight variations in particle size are evident. Selected area electron diffraction (SAED) patterns (Figure 2d,h,l) exhibit ring-like diffraction features. Notably, the CTAB-intercalated EMD sample shows fewer diffuse rings and more voids in the diffraction pattern, indicating reduced crystallinity. Energy-dispersive X-ray spectroscopy confirmed the presence of manganese (Mn) and oxygen (O) in all samples. Furthermore, X-ray photoelectron spectroscopy (XPS) analysis of the TTAB-mediated EMD sample (**Figure 3**) verified the presence of Mn, O, and carbon (C). All binding energies were calibrated using the adventitious C 1s peak at 284.8 eV. The Mn 2p peaks were deconvoluted into multiplets corresponding to Mn^{4+} and Mn^{3+} oxidation states, with Mn $2p_3/_2$ and Mn $2p_1/_2$ peaks located at 641.50 and 653.38 eV, respectively. These results confirm that the electrodeposited material is primarily MnO_2. However, XPS analysis did not detect any bromine species in the TTAB-derived EMD, despite their expected presence due to the surfactant. This absence may be attributed to the limited detection sensitivity of the XPS technique.

The surface area and pore structure characteristics of the EMD samples are presented in Figure S4, Supporting Information. All samples exhibit type IV nitrogen adsorption–desorption isotherms with H2-type hysteresis loops, indicative of mesoporous structures. The Brunauer–Emmett–Teller surface area of pristine EMD is measured at 75 $m^2 g^{-1}$. In comparison, the CTAB- and TTAB-modified EMD samples show enhanced surface areas of ≈90 and 100 $m^2 g^{-1}$, respectively.

2.2. Electrochemical Performance of γ-MnO_2: Three-Electrode Configuration

Figure 4a–c presents the cyclic voltammetry (CV) curves of the EMD samples tested in a 1 M Na_2SO_4 aqueous electrolyte at sweep rates ranging from 2 to 50 mV s^{-1}, within a potential window of 0 to +1 V. CV analysis is a powerful technique for probing the electrochemical behavior of electrode materials.[31] In this study, CV measurements were conducted using a three-electrode setup, where EMD served as the working electrode, platinum as the counter electrode, and Ag/AgCl as the reference. At lower sweep rates (2–10 mV s^{-1}), the CV curves exhibit a nearly rectangular shape, indicating minimal dependance of differential capacitance on electrode potential. However, as the sweep rate increases beyond 20 mV s^{-1}, the curves deviate from this ideal

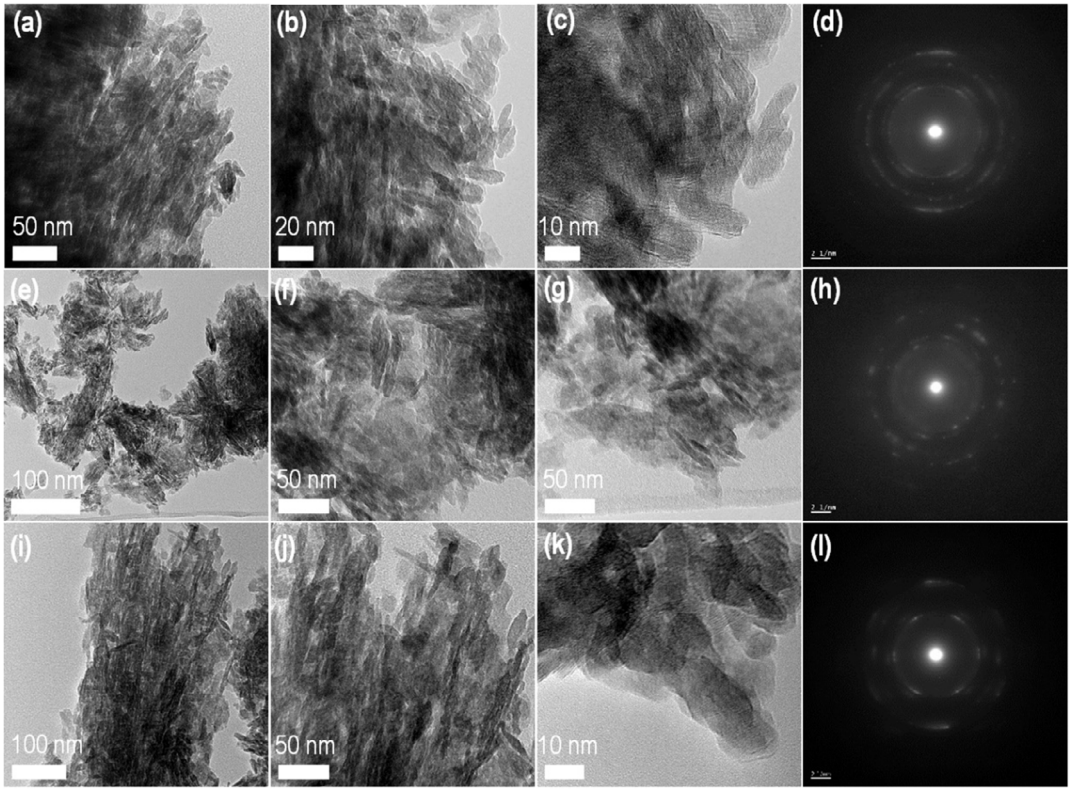

Figure 2. TEM of the pristine electrodeposited manganese dioxide (EMD; a–d) compared with two cationic surfactants added EMD, e–h) cetyltrimethylammonium bromide (CTAB), and i–l) tetradecyltrimethylammonium bromide (TTAB). Images (d,h,l) are showing corresponding SADP images, from regions of interest in (a,e,i).

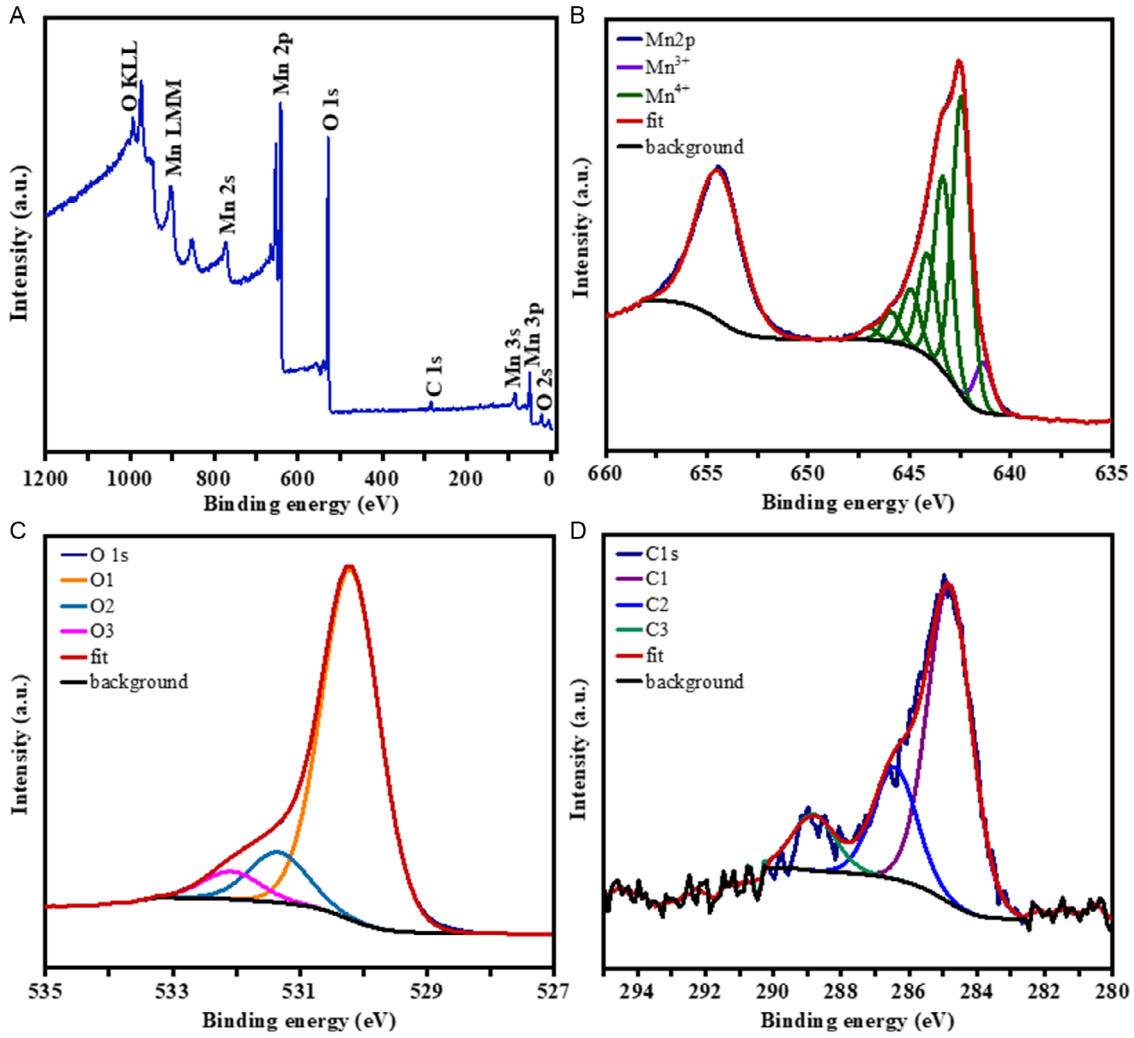

Figure 3. XPS of the cationic surfactant tetradecyltrimethylammonium bromide (TTAB) added EMD. a) Survey spectra, b) Mn 2p spectra, c) O 1s spectra, and d) C 1s spectra.

shape, becoming quasi-elliptical with sharper edges inclined relative to the potential axis, signifying nonequilibrium behavior.[32] At slower scan rates (<10 mV s^{-1}), protons and Na^+ ions have sufficient time to migrate to the EMD surface, desolvate, and adsorb. In contrast, at higher scan rates (≥ 20 mV s^{-1}), polarization effects during desolvation hinder ion adsorption, leading to deviations from ideal capacitive behavior. The area under the CV curves increases with sweep rate, while the specific capacitance decreases, consistent with the limited time available for ion diffusion and adsorption at higher rates. Notably, the TTAB-intercalated EMD exhibits significantly enhanced energy storage, with current responses approximately twice that of pristine EMD and three times that of CTAB-modified samples. These differences are attributed solely to the nature of the surfactant used during synthesis, as all other experimental conditions were held constant (see Experimental Section).

Figure 4d–f and S3, Supporting Information, display the galvanostatic charge–discharge (GCD) curves recorded at current densities of 0.6, 1.3, 3.3, 6.6, 10, and 13.3 A g^{-1}. The GCD profiles are quasi-triangular, lacking distinct anodic or cathodic plateaus, which is characteristic of EDLCs. The absence of redox peaks in both CV and GCD curves confirms the pseudocapacitive nature of the EMD material.[33] Capacitance values were derived from the slope of the voltage–time curves. The voltage increased nearly linearly with time, with slight nonlinearity attributed to faradaic processes involving Mn redox transitions or surface charge rearrangements. The specific capacitances for pristine EMD were 232, 182, 166, 120, 110, and 93 F g^{-1}, while CTAB-modified samples showed reduced values of 124, 109, 83, 66, 50, and 40 F g^{-1}. In contrast, TTAB-modified EMD demonstrated significantly enhanced capacitance values of 478, 400, 333, 280, 240, and 200 F g^{-1}, indicating a greater faradaic contribution and prolonged discharge times. At higher current densities, the capacitance of TTAB-EMD decreased to 42% of its initial value, still outperforming both pristine and CTAB samples, suggesting that ion diffusion into the bulk and inner pores of EMD becomes increasingly limited.[34] Overall, electrochemical supercapacitors offer several advantages over traditional batteries, including high specific power, excellent cycling stability, and near-100% energy efficiency during charge–discharge cycles.

To further evaluate the performance of the single EMD electrode, continuous charge–discharge cycling was conducted at a current density of 3.3 A g^{-1}. The initial and final charge–discharge

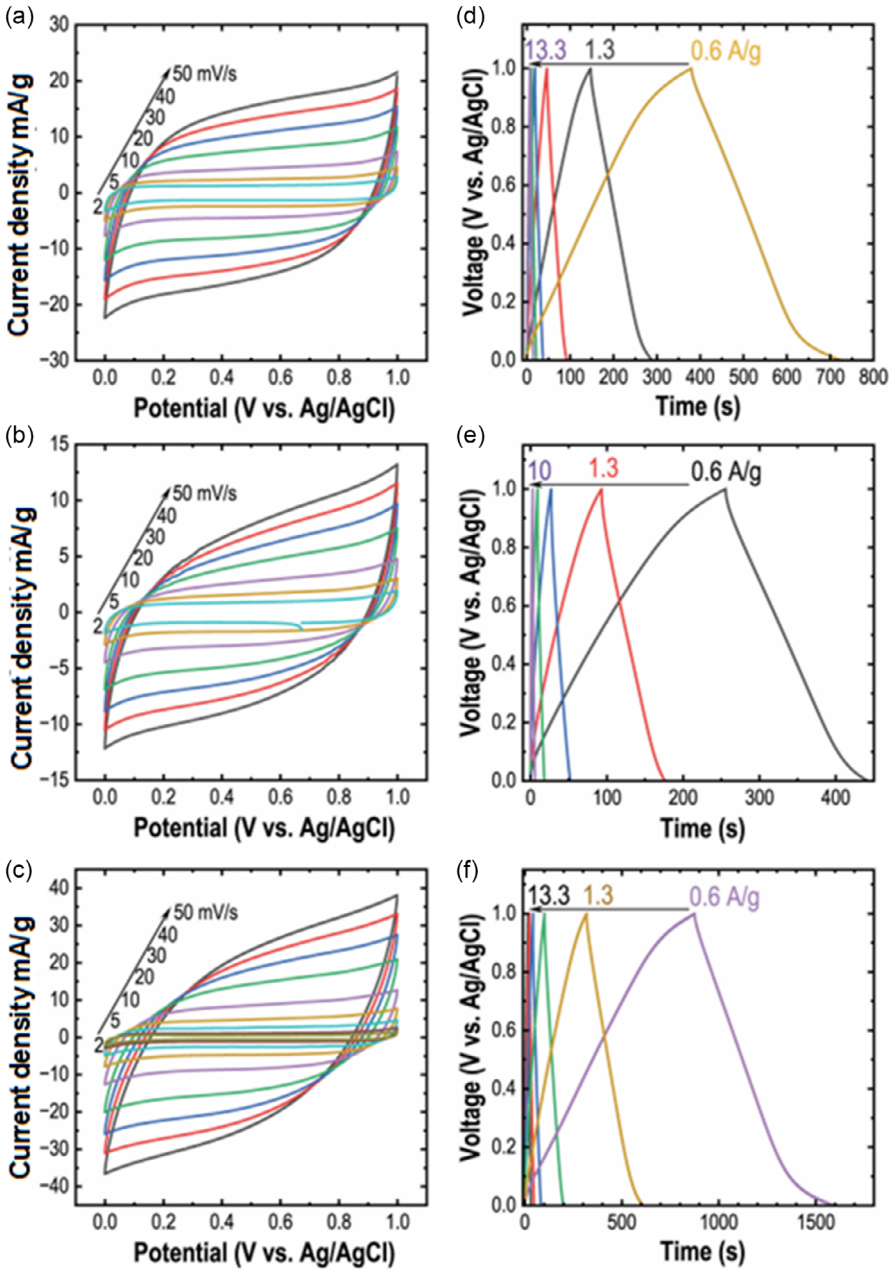

Figure 4. a) CV curves three-electrode configuration of the pristine EMD compared with two cationic surfactants added EMD, b) cetyltrimethylammonium bromide (CTAB), and c) tetradecyltrimethylammonium bromide (TTAB) recorded at various sweep rates indicated in the respective figure. GCD curves, three-electrode configuration of the pristine EMD, d) compared with two cationic surfactants added EMD, e) cetyltrimethylammonium bromide (CTAB), and f) tetradecyltrimethylammonium bromide (TTAB), recorded at various current densities indicated in the respective figure.

curves, recorded after 1000 cycles, are superimposed and presented in **Figure 5**. The near-identical nature of these curves after prolonged cycling indicates excellent reversibility and suggests strong potential for commercial applications. Capacitance retention after 1000 cycles was 93.9%, 98%, and 95.8% for pristine, CTAB-, and TTAB-intercalated EMD, respectively. These results demonstrate the outstanding cycling stability of EMD-based electrodes. Among them, TTAB-intercalated EMD exhibited the highest capacitance, making it a promising candidate for high-efficiency energy storage in supercapacitors. The observed capacitance retention is closely linked to the equivalent series resistance (ESR), as illustrated in the Nyquist plots in Figure 5d. In a basic equivalent circuit model for EDLCs (nonfaradaic systems), the components include series resistance and double-layer capacitance.[35] For carbon-based materials, additional faradaic parallel resistance is present, which encompasses both charge transfer and pseudoresistances. In pseudocapacitors—such as those derived from EMD—this faradaic resistance is inversely related to the overpotential-dependent charge transfer rate.[36] As shown in Figure 5d, CTAB-intercalated EMD exhibits a higher ESR in the high-frequency region, corresponding to the electrode–electrolyte interface. In contrast, TTAB-intercalated

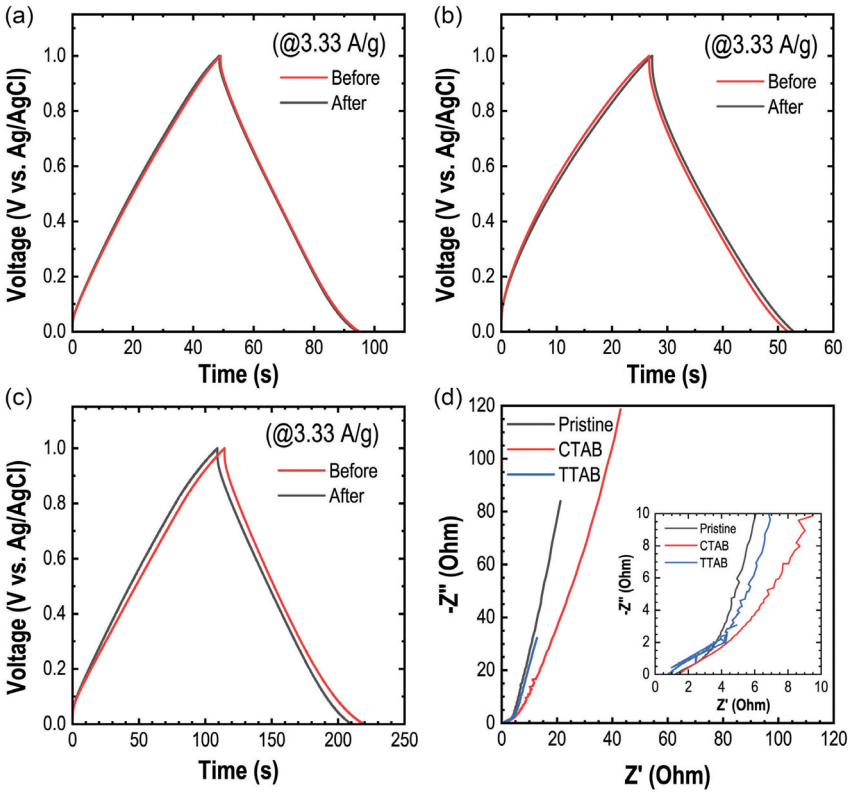

Figure 5. a) GCD curves three-electrode configuration of the pristine EMD compared with two cationic surfactants added EMD, b) cetyltrimethylammonium bromide (CTAB), and c) tetradecyltrimethylammonium bromide (TTAB) recorded at a similar current density of 3.3 A g^{-1} indicating the long-term stability after 1000 cycles. The curves are superimposed for the initial and final cycles, and d) The Nyquist plots of the pristine EMD compared with two cationic surfactants added EMD (b) cetyltrimethylammonium bromide (CTAB), and (c) tetradecyltrimethylammonium bromide (TTAB). The CTAB shows an ill-defined curve.

EMD shows a lower ESR and a near-vertical line approaching 90° in the low-frequency region, indicating superior ion transport and electrodeposition characteristics.

The morphology and crystal structure of the EMD material after cycling were examined to assess its stability. The corresponding FESEM images and XRD patterns are presented in Figure S5, Supporting Information. The crystal structure of the EMD materials remained largely unchanged, regardless of the presence or absence of surfactants. However, the morphology of the cycled pristine (Figure S5a, Supporting Information) material exhibited surface deposits, likely originating from electrolyte ions. In the case of TTAB, both particle size and morphology remained stable before and after cycling (compare Figure 1 and Figure S5c, Supporting Information). In contrast, CTAB-treated samples (Figure S5b, Supporting Information) showed morphological changes, attributed to the irreversible incorporation of surfactant molecules, which were visible on the surface. Five prominent XRD peaks are observed, Figure S5d, Supporting Information, in each sample at distinct 2θ values, approximately at 22°, 37°, 42°, 56°, and 67°. The XRD patterns, recorded both in the absence and presence of surfactants, consistently exhibit the characteristic reflections of γ-MnO_2. These correspond to the (120), (131), (300), (160), and (003) crystallographic planes, respectively. The γ-MnO_2 phase is identified as orthorhombic, in accordance with the JCPDS reference file no. 14-644.

This study reports, for the first time, the synthesis of EMD via electrodeposition with in situ incorporation of cationic surfactants (CTA^+/TTA^+) into the structure. This approach significantly enhances the electrochemical performance for supercapacitor applications. The aggregation behavior of CTAB results in the immobilization of CTA^+ cations and the incorporation of SO_4^{2-} anions from the Na_2SO_4 electrolyte for charge compensation, yielding a specific capacitance of 124 F g^{-1}. In contrast, TTAB surfactants actively participate in redox processes and are replaced by Na^+ ions, leading to a markedly higher capacitance of 478 F g^{-1}. The loosely packed, water-rich bulk structure of the material facilitates faradaic contributions during redox reactions.

The underlying mechanism is attributed to the longer alkyl chain of CTA^+ (C16) compared to TTA^+ (C14), which enhances hydrophobic interactions and promotes greater aggregation. This results in a more compact structure that immobilizes CTA^+ ions, thereby restricting their diffusion and preventing their involvement in redox or ion-exchange processes. Conversely, TTAB surfactants, like CTAB, remain mobile and actively contribute to redox activity. These findings underscore the critical role of surfactant selection in modulating the structural and electrochemical properties of EMD. The introduction of structural defects through targeted surfactant intercalation emerges as a key strategy for optimizing energy storage performance.

2.3. Electronic Structure Analysis

The band structure of γ-MnO_2 was computed using a k-point path that included the high-symmetry points Γ, X, S, Y, Z,

U, R, and T. Specifically, 16k-points were defined with the following coordinates in the Brillouin zone: Γ (0,0,0), X (0.5,0,0), S (0.5,0.5,0), Y (0,0.5,0), Z (0,0,0.5), U (0.5,0,0.5), R (0.5,0.5,0.5), and T (0,0.5,0.5).

For the CTAB/TTAB systems incorporating γ-MnO_2 units, the band structure was analyzed along a more extensive high-symmetry k-point path, including Γ, X, Y, Z, R, T, U, V, and their respective counterparts X′, Y′, Z′, R′, T′, U′, and V′. This path comprised 22 k-points with coordinates: Γ (0,0,0), X (0.5,0,0), Y (0,0.5,0), Z (0,0,0.5), U (0.5,0,0.5), R (0.5,0.5,0.5), T (0,0.5,0.5), V (0.5,0.5,0), and their counterparts X′ (−0.5,0,0), Y′ (0,−0.5,0), Z′ (0,0,−0.5), U′ (−0.5,0,−0.5), R′ (−0.5,−0.5,−0.5), T′ (0,−0.5,−0.5), and V′ (−0.5,−0.5,0). The same plane-wave cutoff and smearing parameters used in the SCF and nonself-consistent field (NSCF) calculations were applied here. The calculated Fermi energy for pristine γ-MnO_2 (two units) was 10.1068 eV. Upon incorporation of CTAB and TTAB, the Fermi energy decreased to −6.2162 and −6.2825 eV, respectively. The corresponding band structures are presented in **Figure 6**. A notable increase in the density of states (DOS) near the Fermi level was observed for γ-MnO_2 upon inclusion of CTAB and TTAB, as shown in **Figure 7**. This enhancement in DOS suggests improved electron and ion transport, which may contribute to enhanced energy storage performance.

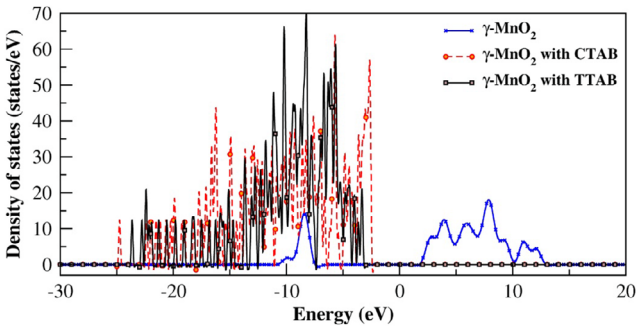

Figure 7. The density of states calculated for 2 units of γ-MnO_2, γ-MnO_2 with CTAB, and γ-MnO_2 with TTAB, respectively.

2.4. Hybrid Device

The analysis of the electronic structure confirms that micelle formation in the electrolyte enhances the density of states, irrespective of the surfactant type. However, electrochemical data obtained using a three-electrode configuration reveal that among the EMD materials synthesized with and without cationic surfactants (CTAB and TTAB), the TTAB-intercalated EMD exhibits superior performance. Consequently, this material was selected for fabricating the hybrid device in a two-electrode system.

In symmetric capacitors, the cell voltage is typically limited to 1 V due to the use of identical electrode materials. To overcome this limitation and improve both cell voltage and energy density, hybrid capacitors have been developed.[37,38] Asymmetric capacitors combine faradaic (EMD) and nonfaradaic (activated carbon) charge storage mechanisms. **Figure 8** presents the CV, charge–discharge (CD), and long-term cycling performance of the hybrid device. The CV curves, recorded at scan rates ranging from 2 to 50 mV s^{-1}, display a quasi-rectangular shape without distinct redox peaks, indicative of pseudocapacitive behavior where current response is largely independent of electrode potential. Even at higher scan rates, the CV profiles maintain their shape, suggesting enhanced ion diffusion and charge transfer facilitated by the hybrid material and the porous structure of activated carbon, which exhibits low internal resistance.[39] The corresponding GCD profiles at various current densities show nearly triangular shapes, characteristic of combined EDLC and pseudocapacitive behavior. Charging and discharging durations were ≈800 s. The specific capacitance values were 106, 88, 60, 26, 15, and 10 F g^{-1} at current densities of 0.4, 0.75, 2, 4, 6, and 8 A g^{-1}, respectively. The device demonstrated excellent long-term stability, retaining 96% of its initial capacitance after 5000 cycles. The initial capacitance of 164 F g^{-1} decreased slightly to 158 F g^{-1} after cycling. At a current of 2 mA, the energy and power densities were calculated to be 59 Wh kg^{-1} and 394 W kg^{-1}, respectively. At 10 mA, these values were 16 Wh kg^{-1} and 5780 W kg^{-1}. These results highlight the dual role of the TTAB surfactant in

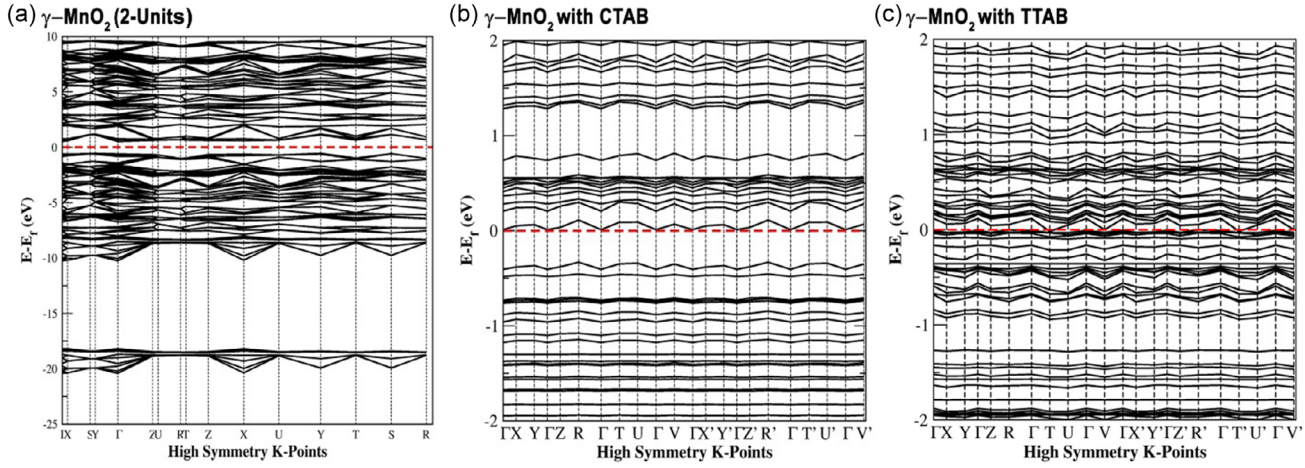

Figure 6. Band structure calculated for a) 2-units of γ-MnO_2, b) γ-MnO_2 with CTAB, and c) γ-MnO_2 with TTAB, respectively.

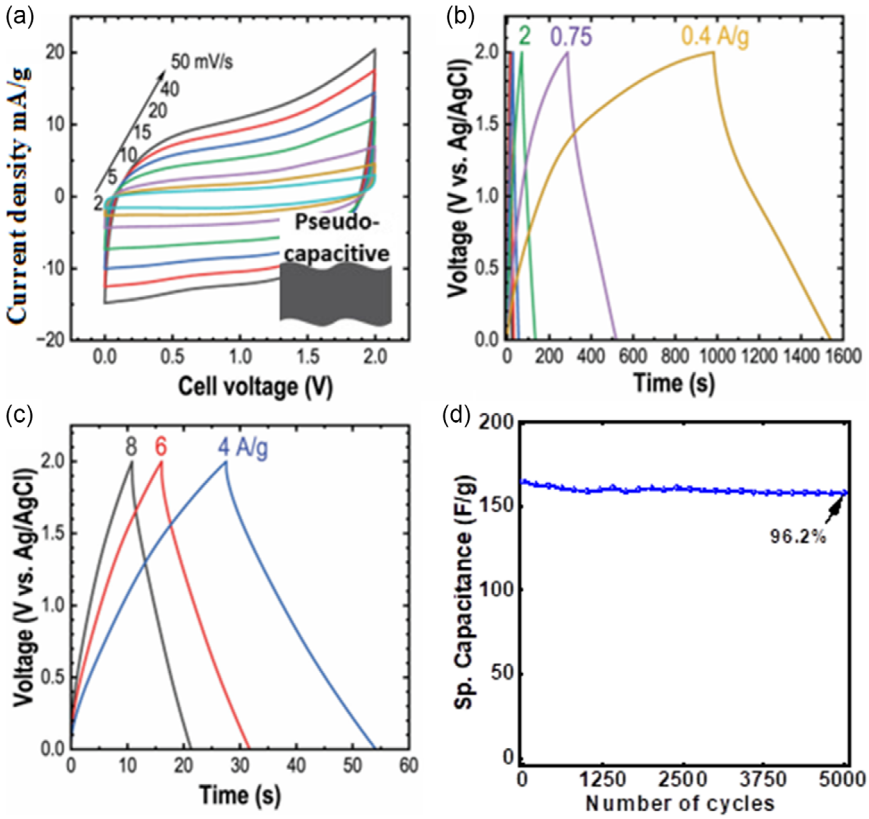

Figure 8. Electrochemical data for the hybrid device (EMD || AC). a) CV, b,c) GCD, and d) long-term cyclability curves of a two-electrode configuration of the best-performed tetradecyltrimethylammonium bromide (TTAB) cationic surfactants added EMD coupled with activated carbon.

the electrolytic bath—not only in stabilizing the material but also in facilitating the scalable synthesis of EMD with intercalated surfactant molecules, thereby enhancing the electrochemical storage properties.

The charge storage behavior of EMD modified with TTAB involves both faradaic and nonfaradaic processes. These mechanisms were analyzed using CV data (**Figure 9**a) at various scan rates, based on the power law relationship described in Equation (2).

$$i = av^b \tag{2}$$

where i is the measured current (A), v is the scan rate (V s^{-1}), and a and b are adjustable parameters.[37,40] The b value, determined from the slope of the log(i) versus log(v) plot (inset of Figure 9a), provides insight into the dominant charge storage mechanism. A b value close to 0.5 indicates diffusion-controlled (faradaic) processes, while values approaching 1 suggest capacitive (nonfaradaic) behavior. At potentials until 1.2 V, b values ranged from 0.5 to 0.65, confirming that charge storage in the EMD material primarily occurs through faradaic processes within the 0–1.2 V potential window. The maximum b value observed was 0.81 at 1.8 V, indicating a predominance of capacitive reactions at higher voltages.

To further quantify the contributions of faradaic and nonfaradaic mechanisms, the current response at a fixed potential was deconvoluted using Equation (3).

$$i(V) = k_1 v + k_2 v^{1/2} \tag{3}$$

Here, $k_1 v$ represents the capacitive (surface-controlled) contribution, and $k_2 v^{1/2}$ corresponds to the diffusion-controlled intercalation process.[37] By rearranging this equation into a linear form (Equation (4)), the values of k_1 and k_2 were extracted from the slope and intercept of the linear fit, respectively.

$$i(V)/v^{1/2} = k_1 v^{1/2} + k_2 \tag{4}$$

Figure 9b illustrates this analysis, and the resulting values were used to calculate the relative contributions of each mechanism at different scan rates, as shown in Figure 9c. As the scan rate increased, the capacitive contribution also increased, while the faradaic contribution decreased. Specifically, the capacitive contributions of the charge storage at scan rates of 2, 5, 10, 20, 40, and 50 mV s^{-1} were calculated to be 20%, 30%, 38%, 45%, 50%, and 55%, respectively. These findings are consistent with the CV profiles of TTAB-modified EMD, which retained pseudocapacitive characteristics to some extent even at higher scan rates (≥20 mV s), indicating suitability for high-rate charge/discharge applications. The Ragone plot (Figure 9d) of the EMD||AC device demonstrates a specific capacitance of 106 F g^{-1}, delivering an energy density of 40 Wh Kg^{-1} at a power density of 540 W Kg^{-1}. Impressively, the device maintains an energy density of 16 Wh Kg^{-1} even at a high-power density of 5780 W Kg^{-1}. Notably, the obtained performance metrics surpass those reported for surfactant-assisted MnO_2 systems in the literature.[24,41,42]

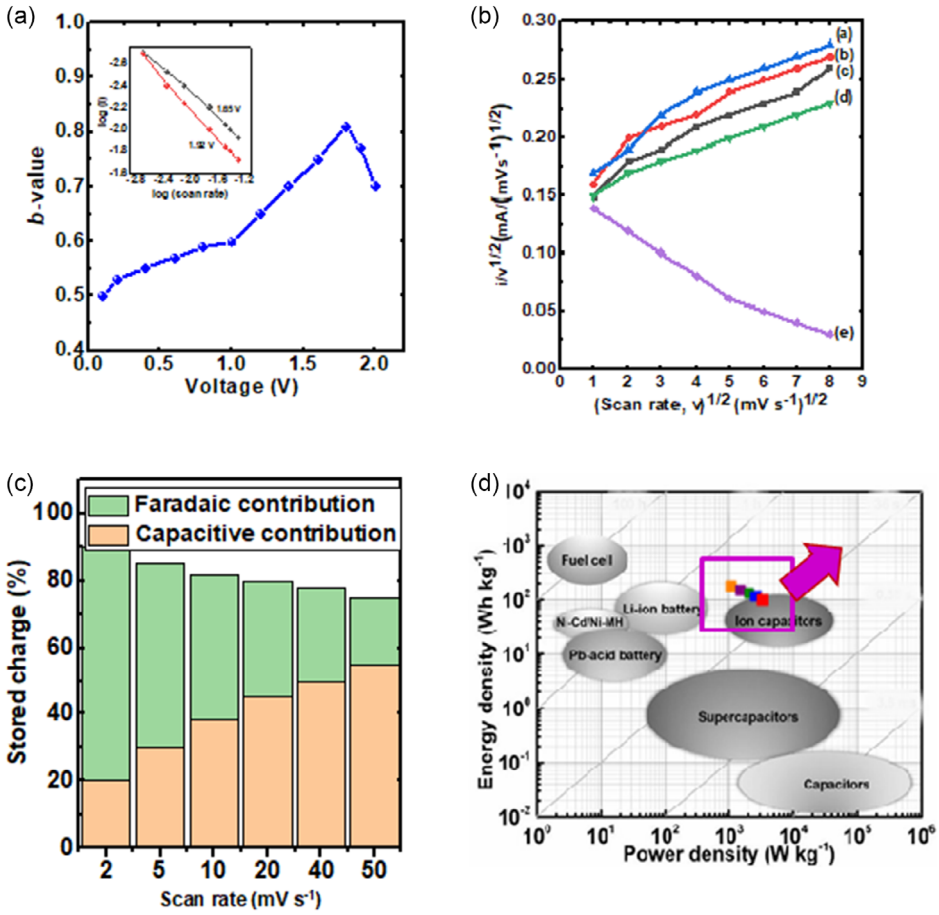

Figure 9. a) Variation of b-values for γ-MnO_2 with TTAB as a function of voltage during anodic sweeps at scan rates of 2, 5, 10, 20, 40, and 50 mV s^{-1}. The inset displays the corresponding power-law relationship, showing log(current) versus log(scan rate). b) Analysis based on Equation (2) across different voltage regimes: a) 0.2 V, b) 0.5 V, c) 1.2 V, d) 1.7 V, and e) 2.0 V. c) Deconvolution of capacitive and diffusion-controlled contributions to the total charge storage. d) Ragone plot comparing the energy and power densities of γ-MnO_2 with TTAB at various current densities against other electrochemical energy storage systems, highlighting the superior performance of the proposed sodium-ion capacitor.

3. Conclusions

EMD in the γ-MnO_2 phase was electrodeposited from an aqueous $MnSO_4$ solution in the presence and absence of various cationic surfactants. The incorporation of surfactant molecules during deposition introduced structural defects into the EMD, which enhanced its charge transfer efficiency, specific capacitance, and ion affinity—collectively improving its electrochemical energy storage performance. The observed pseudocapacitive behavior, as evidenced by deviations in CV and charge-discharge profiles, is attributed to the reversible redox transitions between Mn^{3+} and Mn^{4+} within the γ-MnO_2 structure. During electrodeposition, cetyltrimethylammonium (CTA^+) ions were immobilized within the EMD matrix, while tetradecyltrimethylammonium (TTA^+) ions facilitated defect formation and ion exchange with Na^+ for charge compensation. This mechanism enabled the TTAB-modified EMD to exhibit prolonged discharge times and enhanced capacitance. Electronic structure analysis revealed a decrease in Fermi energy and an increase in the density of states for CTAB/TTAB-modified γ-MnO_2, indicating improved electronic conductivity. At a constant current of 0.6 A g^{-1}, the TTAB-modified EMD delivered a specific capacitance of 478.6 F g^{-1}, significantly outperforming the CTAB-modified (124 F g^{-1}) and pristine (223 F g^{-1}) samples. This performance difference is attributed to the shorter hydrophobic tail of TTAB compared to CTAB, which influences their aggregation behavior and defect formation. A hybrid device constructed with TTAB-EMD and activated carbon (AC) achieved a specific capacitance of 106 F g^{-1} at 0.4 A g^{-1}. These findings demonstrate that the choice of surfactant cations plays a critical role in regulating defect formation and aggregation, thereby enhancing electrochemical energy storage capabilities.

4. Experimental Section

Materials

All chemicals used in the experiments were procured from Sigma–Aldrich. Manganese sulfate monohydrate ($MnSO_4{\cdot}H_2O$, 99.5%) served as the manganese source for the electrodeposition process. $MnSO_4{\cdot}H_2O$ and concentrated sulfuric acid (H_2SO_4, 98%) were dissolved in deionized (DI) water to prepare the electrolyte solution. The concentrations of $MnSO_4{\cdot}H_2O$ and H_2SO_4 in the electrolytic bath were 50 g L^{-1} and 25 g L^{-1}, respectively.

Experimental Setup and Synthesis

The electrodeposition process was conducted in a 500 mL glass beaker, sealed with a precision-machined PTFE lid (99.99% purity). A pure lead (Pb) disk served as the anode, while a stainless steel 304 (SS304) disk functioned as the cathode. Prior to deposition, both electrodes were mechanically polished using sandpaper, thoroughly rinsed with DI water to eliminate surface contaminants, and gently dried with lint-free tissues. Following preparation, the electrodes were assembled in the electrolytic bath, and electrical connections were established. The electrolyte solution—comprising manganese sulfate monohydrate ($MnSO_4{\cdot}H_2O$) and concentrated sulfuric acid (H_2SO_4) in appropriate ratios—was continuously stirred using a Teflon-coated magnetic stir bar to ensure homogeneity. A series of galvanostatic electrodeposition experiments was performed under identical conditions, including fixed deposition time and current density. However, different surfactants were introduced as additives in varying concentrations to evaluate their influence on deposition characteristics. The process parameters were subsequently optimized to achieve maximum performance metrics. Throughout the experiments, the bath temperature was maintained within the range of 90–95 °C. The proposed electrochemical reactions occurring in the bath during deposition are outlined in Equation (5)–(7).

$$Mn^{2+} + 2H_2O \rightarrow MnO_2 + 4H^+ + 2e^- \quad \text{Anode (Pb)} \tag{5}$$

$$2H^+ + 2e^- \rightarrow H_2 \quad \text{Cathode (SS)} \tag{6}$$

$$Mn^{2+} + 2H_2O \rightarrow MnO_2 + 2H^+ + H_2 \quad \text{Overall} \tag{7}$$

After completing the electrodeposition process, the Pb electrode was promptly removed from the electrolyte bath. The electrodeposited material was thoroughly rinsed with DI water to eliminate any residual electrolytes. It was then dried overnight in an oven. The resulting manganese dioxide (MnO_2), referred to as EMD and shown in Figure S1, Supporting Information, was carefully scraped from the Pb electrode surface to prevent contamination from lead. The collected EMD fragments were finely ground into a powder. This powdered EMD was repeatedly rinsed to remove any remaining electrolyte and subsequently dried in an oven at 80 °C overnight.

Pristine EMD was synthesized using a surfactant-free electrolyte. For the preparation of surfactant-intercalated EMD, 30 mg L^{-1} of either cetyltrimethylammonium bromide (CTAB) or tetradecyltrimethylammonium bromide (TTAB) was uniformly dispersed in the electrolyte. The critical micelle concentrations (CMC) of CTAB and TTAB in aqueous media are ≈1.3 and 4.1 mol dm^{-3}, respectively. During electrodeposition, the hydrophobic nature of the surfactants facilitated their intercalation into the MnO_2 deposit, thereby influencing the nucleation and growth of EMD on the Pb substrate.

Both CTAB and TTAB surfactants were investigated at varying concentrations,15, 30, and 60 mg L^{-1}. Optimal performance was observed at 30 mg L^{-1} for TTAB. During the electrodeposition process, an initially rough surface formed on the Pb substrate due to nucleation. In the absence of surfactants, the EMD adhered strongly to the substrate, making removal difficult. However, the presence of TTAB significantly reduced interfacial tension, allowing the EMD to be easily detached. This simple and cost-effective approach not only facilitates EMD recovery but also minimizes Pb contamination, enhancing the scalability of the process. Nevertheless, excessive TTAB disrupts the EMD structure, necessitating careful concentration optimization. In contrast, CTAB tends to aggregate at lower concentrations, and its optimal performance was also achieved at 30 mg L^{-1}.

Physical Characterization

The surface morphology and elemental composition of the electrodeposited MnO_2 samples were characterized using (FESEM, Zeiss NEON 40EsB). Transmission electron microscopy (TEM) analysis was conducted with a JEOL 2200FS TEM operating at 200 kV. TEM specimens were prepared by dispersing a small quantity of EMD powders in ethanol, followed by grinding in an agate mortar and pestle. The resulting suspension was drop-cast onto a holey carbon film supported on a copper TEM grid. XPS was performed using a Kratos Ultra DLD instrument equipped with a monochromatic Al Kα X-Ray source to analyze the EMD sample synthesized with TTAB surfactant mediation.

Electrochemical Analysis

The electrochemical charge/discharge measurements were conducted using a battery analyzer in both three-electrode and two-electrode configurations. The electrochemical cell comprised a cathode and an anode immersed in an aqueous 1 M sodium sulfate (Na_2SO_4) electrolyte. The cathode was prepared using a composite of (EMD, 75 wt%), carbon black (15 wt%), and polyvinylidene fluoride (PVDF, 10 wt%), thoroughly mixed in an agate mortar with 0.3–0.4 mL of N-methyl-2-pyrrolidone (NMP). The resulting slurry was coated onto a 1 cm^2 graphite sheet and dried at 55 °C for 1.5 h. The mass of the active material (EMD) was determined by measuring the weight of the graphite electrode before and after coating. CV and electrochemical impedance spectroscopy (EIS) were performed using a BioLogic VSP-300 system in a three-electrode setup. The working electrode was the graphite sheet coated with the active material, with a platinum wire as the counter electrode and an Ag/AgCl electrode as the reference. All measurements were carried out in 1 M Na_2SO_4 electrolyte. CV experiments were conducted within a potential window of 0.0 to 1.0 V (vs. Ag/AgCl) at scan rates ranging from 2 to 50 mV s^{-1}. EIS measurements were recorded over a frequency range of 100 kHz to 1 mHz with an amplitude of 5 mV.

Computational Details

Electronic structure calculations were performed using density functional theory calculations with the Quantum ESPRESSO package[36] for the 2-units of γ-MnO_2.The PBEsol Perdew–Burke–Ernzerhof for solids exchange-correlation functional was employed to describe the electron–lectron interactions. The pseudopotentials used were obtained from the Quantum ESPRESSO pseudopotential library. A plane-wave basis set with a kinetic energy cutoff of 40 Ry for the wavefunctions and 400 Ry for the charge density was used. The Brillouin zone was sampled using a Monkhorst-Pack grid of $4 \times 8 \times 12$ k-points. The atomic positions were optimized using the Broyden–Fletcher–Goldfarb–Shanno algorithm,[43] with convergence thresholds for total energy and forces set to 10^{-4} Ry and 10^{-3} Ry/Bohr, respectively. The self-consistent field (SCF) cycle was considered converged when the difference in electronic density between iterations was below 1.0×10^{-8}. Smearing of the occupations was applied using the Methfessel–Paxton method with a smearing width of 0.05 Ry. Subsequent NSCF calculations were performed using the optimized geometry (see Figure S2, Supporting Information), and the Brillouin zone was sampled with a denser $8 \times 8 \times 12$ k-point grid. For MnO_2 system incorporating CTAB and TTAB, a plane-wave basis set with a kinetic energy cutoff of 10 Ry for wavefunctions and 50 Ry for charge density was employed. The Brillouin zone was initially sampled with a $1 \times 1 \times 1$ k-point grid for the SCF calculations, with convergence achieved when the electronic density difference between iterations fell below 1.0×10^{-4}. Occupation smearing was applied using the Methfessel–Paxton method with a smearing width of 0.01 Ry. For NSCF calculations, a denser $3 \times 3 \times 3$ k-point grid was used.

Acknowledgements

M.M. acknowledges the Winston Churchill Fellowship to learn globally and inspire locally. This work was partially supported by the Japan Society for the Promotion of Science (JSPS) KAKENHI grant nos. JP20H00392 and JP23H05459.

Open access publishing facilitated by Murdoch University, as part of the Wiley - Murdoch University agreement via the Council of Australian University Librarians.

Conflict of Interest

The authors declare no conflict of interest.

Data Availability Statement

The data that support the findings of this study are available from the corresponding author upon reasonable request.

Keywords: depositions · electrolysis · energy · manganese dioxides · storage · surfactant

[1] M. Winter, R. J. Brodd, *Chem. Rev.* **2004**, *104*, 4245.
[2] L. Liu, Y. Zhang, Y. Song, Y. Gu, H. Pang, R. Zhu, *Inorganic Chem.* **2024**, *63*, 10324.
[3] R. Zhu, L. Liu, G. Zhang, Y. Zhang, Y. Jiang, H. Pang, *Nano Energy* **2024**, *122*, 109333.
[4] R. Zhu, L. Liu, G. Zhang, Y. Xu, Y. Gu, H. Pang, *Coord. Chem. Rev.* **2025**, *532*, 216498.
[5] F. Wang, L. Chen, J. Wei, C. Diao, F. Li, C. Du, Z. Bai, Y. Zhang, O. L. Malyi, X. Chen, Y. Tang, X. Bao, *Energy Environ. Sci.* **2025**, *18*, 4312.
[6] F. Wang, Z. Jiang, Y. Zhang, Y. Zhang, J. Li, H. Wang, Y. Jiang, G. Xing, H. Liu, Y. Tiang, *eScience* **2024**, *4*, 100181.
[7] F. Wang, J. Lee, L. Chen, G. Zhang, S. He, J. Han, J. Ahn, J. Y. Cheong, S. Jiang, I. I.-D. Kim, *ACS Nano* **2023**, *17*, 8866.
[8] F. Wang, J. Y. Cheong, J. Lee, J. Ahn, G. Duan, H. Chen, Q. Zhang, I. I.-D. Kim, S. Jiang, *Adv. Funct. Mater.* **2021**, *31*, 2101077.
[9] L. Chen, F. Wang, Z. Tian, H. Guo, C. Cai, Q. Wu, H. Du, K. Liu, Z. Hao, S. He, G. Duan, S. Jiang, *Small* **2022**, *18*, 2201307.
[10] A. Shuja, H. R. Khan, I. Murtaza, S. Ashraf, Y. Abid, F. Farid, F. Sajid, *J. Alloys Compds.* **2024**, *1009*, 176924.
[11] E. Muchuweni, E. T. Mambeshara, C. M. Muliva, T. S. Sathiaraj, *J. Energy Storage* **2023**, *73*, 109013.
[12] M. Pathak, D. Bhatt, R. C. Bhatt, B. S. Bohra, G. Tatrari, S. Rana, M. C. Arya, N. G. Sahoo, *Chem. Rec.* **2023**, *24*, e202300236.
[13] A. Muzaffar, M. B. Ahamed, C. M. Hussain, *Functionalized Nanomaterials Based Supercapacitor. Materials Horizons: From Nature to Nanomaterials* (Eds: C. M. Hussain, M. B. Ahamed), Springer, Singapore **2024**, pp. 631–651.
[14] Y. Zhao, Z. Geng, W. Sun, *Energy Technol.* **2023**, *11*, 2300373.
[15] J. Wu, D. Zhu, Y. Pan, J. Prabowo, L. Wei, Y. Chen, *Adv. Sci.* **2024**, *11*, 2408997.
[16] Z. Li, X. Wang, L. Zhao, F. Chi, C. Gao, Y. Wang, M. Yan, Q. Zhou, M. Zhao, X. Wang, J. Wang, M. Yuan, M. Wu, L. Wang, Y. Zhao, L. Qu, *Nat. Commun.* **2022**, *13*, 6359.
[17] Y. Chabre, J. Pannetier, *Progr. Solid State Chem.* **1995**, *23*, 1.
[18] J. Shin, J. K. Seo, Y. S. Meng, *Int. Mater. Rev.* **2020**, *65*, 356.
[19] Z. You, W. Hua, H. Liu, J.-G. Wang, *Chin. Chem. Lett.* **2023**, *34*, 107525.
[20] F. Wang, Y. Zheng, Q. Chen, Z. Yan, D. Lan, E. Lester, T. Wu, *Coord. Chem. Rev.* **2024**, *500*, 215537.
[21] K. Wickramaarachchi, M. Minakshi, D. J. Henry, X. Gao, *ACS Appl. Energy Mater.* **2021**, *4*, 7040.
[22] S. Devaraj, N. Munichandraiah, *J. Phys. Chem. C* **2008**., *112*, 4406.
[23] Y. He, Z. Kang, J. Li, Y. Li, X. Tian, *Ind. Chem. Mater.* **2023**, *1*, 312.
[24] S. Devaraj, N. Munichandraiah, *Electrochem. Solid State Lett.* **2005**, *8*, A373.
[25] M. Alam, M. R. Malla, S. Rana, M. A. Rub, N. Azum, A. Hoque, S. E. Kabir, *J. Mol. Liq.* **2019**, *285*, 766.
[26] M. A. Hoque, M. O. F. Patoary, M. M. Rashid, M. R. Molla, M. A. Rub, *J. Sol. Chem.* **2017**, *46*, 682.
[27] H. M. Lee, S. W. Cho, C. J. Song, H. J. Kang, B. J. Kwon, C. K. Kim, *Electrochim. Acta* **2015**, *160*, 50.
[28] M. Nakayama, M. Shamoto, A. Kamimura, *Chem. Mater.* **2010**, *22*, 5887.
[29] M. Nakayama, R. Hoyashita, H. Komatsu, E. Muneyama, K. Shoda, A. Kunishige, *Langmuir* **2007**, *23*, 3462.
[30] F. Cheng, J. Liang, Z. Tao, J. Chen, *Chem. Mater.* **2010**, *22*, 898.
[31] D. A. Bograchev, Y. M. Volfkovich, S. Martemianov, *J. Electroanal. Chem.* **2023**, *935*, 117322.
[32] E. Lim, C. Jo, J. Lee, *Nanoscale* **2016**, *8*, 7827.
[33] E. Taer, R. Taslim, M. P. Sugianto, W. S. M. Mukhlis, *Int. J. Power Electron. Drive Syst.* **2018**, *9*, 1263.
[34] J. G. Reynolds, T. R. Graham, C. I. Pearce, *J. Mol. Liq.* **2022**, *360*, 119441.
[35] S. Yoon, C. W. Lee, S. M. Oh, *J. Power Sources* **2010**, *195*, 4391.
[36] P. Giannozzi, S. Baroni, N. Bonini, M. Calandra, R. Car, C. Cavazzoni, D. Ceresoli, G. L. Chiarotti, M. Cococcioni, I. Dabo, A. Dal Corso, S. de Gironcoli, S. Fabris, G. Fratesi, R. Gebauer, U. Gerstmann, C. Gougoussis, A. Kokalj, M. Lazzeri, L. Martin-Samos, N. Marzari, F. Mauri, R. Mazzarello, S. Paolini, A. Pasquarello, L. Paulatto, C. Sbraccia, S. Scandolo, G. Sclauzero, A. P Seitsonen, A. Smogunov, P. Umari, R. M. Wentzcovitch, *J. Phys.: Condensed Matter* **2009**, *21*, 395502.
[37] T. Schoetz, L. W. Gordon, S. Ivanov, A. Bund, D. Mandler, R. J. Messinger, *Electrochim. Acta* **2022**, *412*, 140072.
[38] S. Kaipannan, S. Marappan, *Sci. Rep.* **2019**, *9*, 1.
[39] D. Shrestha, *Mater. Sci. Energy Technol.* **2021**, *5*, 353.
[40] S. Yadav, N. Kurra, *Small*, https://orcid.org/doi.org/10.1002/smll.202503657.
[41] Y. Sun, H. Dang, N. Huang, D. Wang, C. Liang, *J. Appl. Biomater. Funct. Mater.* **2017**, *15*, 7.
[42] H. Soltani, H. Bahiraei, S. Ghasemi, M. Hashmepour, *Heliyon* **2024**, *21*, e41427.
[43] R. H. Byrd, J. Nocedal, R. B. Schnabel, *Mathemat. Prog.* **1994**, *63*, 129.

Manuscript received: May 13, 2025
Revised manuscript received: June 30, 2025
Version of record online: July 21, 2025